

Bi-allelic Variations of *SMO* in Humans Cause a Broad Spectrum of Developmental Anomalies Due to Abnormal Hedgehog Signaling

Thuy-Linh Le,¹ Yunia Sribudiani,^{2,3,21} Xiaomin Dong,^{4,5,21} Céline Huber,⁶ Chelsea Kois,⁷ Geneviève Baujat,^{6,8} Christopher T. Gordon,¹ Valerie Mayne,⁹ Louise Galmiche,¹⁰ Valérie Serre,¹¹ Nicolas Goudin,¹² Mohammed Zarhrate,¹³ Christine Bole-Feysot,¹³ Cécile Masson,¹⁴ Patrick Nitschke,¹⁴ Frans W. Verheijen,² Lynn Pais,¹⁵ Anna Pelet,¹ Simon Sadedin,^{4,5} John A. Pugh,⁷ Natasha Shur,¹⁶ Susan M. White,¹⁷ Salima El Chehadeh,¹⁸ John Christodoulou,^{4,5} Valérie Cormier-Daire,^{6,8} R.M.W. Hofstra,² Stanislas Lyonnet,^{1,8} Tiong Yang Tan,¹⁷ Tania Attié-Bitach,^{8,19} Wilhelmina S. Kerstjens-Frederikse,²⁰ Jeanne Amiel,^{1,8} and Sophie Thomas^{1,*}

The evolutionarily conserved hedgehog (Hh) pathway is essential for organogenesis and plays critical roles in postnatal tissue maintenance and renewal. A unique feature of the vertebrate Hh pathway is that signal transduction requires the primary cilium (PC) where major pathway components are dynamically enriched. These factors include smoothened (*SMO*) and patched, which constitute the core reception system for sonic hedgehog (*SHH*) as well as GLI transcription factors, the key mediators of the pathway. Here, we report bi-allelic loss-of-function variations in *SMO* in seven individuals from five independent families; these variations cause a wide phenotypic spectrum of developmental anomalies affecting the brain (hypothalamic hamartoma and microcephaly), heart (atrioventricular septal defect), skeleton (postaxial polydactyly, narrow chest, and shortening of long bones), and enteric nervous system (aganglionosis). Cells derived from affected individuals showed normal ciliogenesis but severely altered Hh-signal transduction as a result of either altered PC trafficking or abnormal activation of the pathway downstream of *SMO*. In addition, Hh-independent GLI2 accumulation at the PC tip in cells from the affected individuals suggests a potential function of *SMO* in regulating basal ciliary trafficking of GLI2 when the pathway is off. Thus, loss of *SMO* function results in abnormal PC dynamics of key components of the Hh signaling pathway and leads to a large continuum of malformations in humans.

Introduction

Hedgehog (Hh) signaling is a key evolutionarily conserved pathway during development and patterning of most organs. A unique feature of the vertebrate Hh pathway is that the primary cilium (PC) is critical for signal transduction.¹ PC is a microtubule-based organelle emanating from the surface of most cells² in which the components of the Hh pathway are enriched dynamically in response to Hh ligand. In the absence of Hh ligand, its receptor patched 1 (PTCH1) localizes to the PC, where it inhibits smoothened (*SMO*), a second transmembrane protein belonging to the class F family of G-protein coupled receptors (GPCRs). Binding of sonic hedgehog (*SHH*) to PTCH1 leads

to the exit of PTCH1 and the entry of *SMO* into the PC, where *SMO* activation culminates in GLI-dependent transcriptional activities.^{3,4} In mammals, the GLI family consists of three members (GLI1, GLI2, and GLI3) that shift between activating (GLI^A) and repressive (GLI^R) forms to shape the Hh response. When the pathway is off, GLI3^R is the predominant repressor of Hh target genes, whereas GLI2^A is the predominant activator when the pathway is on.⁵

In humans, deregulation of the Hh pathway leads to both malformations and cancers. Heterozygous germline mutations in *SHH* [MIM: 600725] and *PTCH1* [MIM: 300828] cause holoprosencephaly, whereas somatic or germline truncating *PTCH1* mutations can cause basal

¹Université de Paris, *Imagine* Institute, Laboratory of Embryology and Genetics of Malformations, INSERM UMR 1163, 75015 Paris, France; ²Department of Clinical Genetics, Erasmus Medical Center, 3015 GD Rotterdam, the Netherlands; ³Department of Biomedical Sciences, Division of Biochemistry and Molecular Biology, Faculty of Medicine, Universitas Padjadjaran, Bandung 40132, Indonesia; ⁴Brain and Mitochondrial Research Group, Murdoch Children's Research Institute, Royal Children's Hospital, 50 Flemington Rd, Parkville VIC 3052, Australia; ⁵Department of Paediatrics, University of Melbourne, Melbourne, 3010 Victoria, Australia; ⁶Université de Paris, *Imagine* Institute, Laboratory of Molecular and Physiopathological Bases of Osteochondrodysplasia, INSERM UMR 1163, 75015 Paris, France; ⁷Albany Medical Center, 43 New Scotland Ave, Albany, NY 12208, USA; ⁸Fédération de Génétique, Hôpital Necker-Enfants Malades, Assistance Publique Hôpitaux de Paris, 75015 Paris, France; ⁹Department of Medical Imaging, Royal Children's Hospital, Melbourne, Australia 3052; ¹⁰Department of Pathology, Hôpital Necker-Enfants Malades, Assistance Publique Hôpitaux de Paris, 75015 Paris, France; ¹¹Université de Paris, Institut Jacques Monod, UMR7592 CNRS, 15 Rue Hélène Brion, 75013 Paris, France; ¹²Université de Paris, *Imagine* Institute, Cell Imaging, INSERM UMR 1163, 75015 Paris, France; ¹³Université de Paris, *Imagine* Institute, Structure Fédérative de Recherche Necker, Genomic Platform, INSERM UMR 1163 and INSERM US24, Centre National de la Recherche Scientifique UMS3633, 75015 Paris, France; ¹⁴Université de Paris, *Imagine* Institute, Bioinformatics Platform, INSERM UMR 1163, 75015 Paris, France; ¹⁵Center for Mendelian Genomics, Broad Institute of MIT and Harvard, 415 Main St, Cambridge, MA 02142, USA; ¹⁶Children's National, 111 Michigan Ave NW, Washington, D.C. 20010, USA; ¹⁷Victorian Clinical Genetics Services, Murdoch Children's Research Institute and Department of Pediatrics, University of Melbourne, Melbourne, Australia 3052; ¹⁸Service de Génétique Médicale, Hôpital de Hautepierre, 67098 Strasbourg, France; ¹⁹Université de Paris, *Imagine* Institute, Laboratory of Genetics and Development of the Cerebral Cortex, INSERM UMR 1163, 75015 Paris, France; ²⁰Department of Genetics, University Medical Centre Groningen, Hanzelplein 1, 9713 GZ Groningen, the Netherlands

²¹These authors contributed equally to this work

*Correspondence: sophie.thomas@inserm.fr

<https://doi.org/10.1016/j.ajhg.2020.04.010>.

© 2020 American Society of Human Genetics.



cell nevus syndrome (BCNS [MIM: 109400]), also called Gorlin syndrome. Monoallelic germline variations in *SUFU* [MIM: 607035] can also cause BCNS, whereas bi-allelic hypomorphic mutations can cause Joubert syndrome (JBTS [MIM: 213300]). Bi-allelic *GLI1* [MIM: 165220] mutations lead to a phenotypic spectrum ranging from isolated postaxial polydactyly to a broader phenotype overlapping Ellis-van Creveld syndrome (EVC [MIM: 225500]).⁶ Germline heterozygous truncating variants in *GLI2* [MIM: 165230] can cause Culler-Jones syndrome (CJS [MIM: 615849]), associating postaxial polydactyly, and hypopituitarism or holoprosencephaly (HPE9 [MIM: 610829]).^{7,8} Germline heterozygous loss-of-function mutations in *GLI3* [MIM: 165240] are reported in Greig cephalopolysyndactyly syndrome (GCPs [MIM: 175700]) and isolated polydactyly, whereas frameshift mutations located in the middle third of *GLI3* lead to constitutive *GLI3^R* and cause Pallister-Hall syndrome (PHS [MIM: 146510]). Finally, activating somatic missense mutations in *SMO* [MIM: 601500] are found in sporadic basal cell carcinoma (BCC, [MIM: 605462]), medulloblastoma, and in Curry-Jones syndrome (CRJS [MIM: 601707]).^{8,9}

Here, we identified bi-allelic loss-of-function *SMO* variations leading to severely altered Hh-signal transduction and causing pleiotropic developmental anomalies affecting the brain, heart, enteric nervous system (ENS), and skeletal development including postaxial polydactyly as a consistent feature. *SMO* is thus a novel example of a key Hh pathway component for which loss-of-function and activating mutations can cause developmental disorders and cancer, respectively.

Material and Methods

Affected Individuals

Informed consent was obtained for all participating families, and the study was approved by the ethical committee of Paris Ile de France II. Family 2 was recruited via GeneMatcher.¹⁰

Whole-Exome Sequencing

Genomic DNA was extracted from peripheral blood samples. In brief, Agilent SureSelect libraries were prepared from 3 µg of genomic DNA sheared with a Covaris S2 ultrasonicator. Exome capture was performed with the 51 Mb SureSelect Human All Exon kit V5 (Agilent technologies), and sequencing was carried out with a HiSeq2500 (Illumina) machine. After demultiplexing, paired-end sequences were mapped on human genome reference (NCBI build37/hg19 version) via the Burrows-Wheeler Aligner (Illumina). Downstream processing was carried out with the Genome Analysis Toolkit (GATK), SAMtools, and Picard Tools according to documented best practices from the Broad Institute. An in-house software tool (PolyWeb) was used for annotation (based on Ensembl release 71) and filtration of variants according to relevant genetic models. We excluded known variants listed in the public databases dbSNP (build 135), the Exome Variant Server (release ESP6500SI-V2), and the 1000 Genomes variants (release date 21-05-2011) as well as variants previously identified in “in-house” exomes. Then we selected for variants affecting splice sites

or coding regions (non-synonymous substitutions, insertions, or deletions). Targeted resequencing was performed as described previously.¹¹ Sanger sequencing with the primers described in Table S2 was performed so that the NGS findings and the segregation of the mutation within all the families could be validated.

Cell Culture

Fibroblasts were obtained from skin biopsies of affected individuals and cultured in Optimem supplemented with 10% FBS, 100 U/mL penicillin, and 100 mg/mL streptomycin (all from Life Technologies). Starving the cells in serum-free Optimem for 24 h induced ciliogenesis.

For SHH pathway induction, either recombinant human SHH (rhSHH, R&D Systems, Cat: 8908-SH-005) or smoothened agonist (SAG, Cat: sc-202814) was used. rhSHH was used at a final concentration of 100 µg/mL, for 24 h, after 48 h serum starvation, and SAG was used at final concentration of 10 µg/mL, for 24 h, after 48 h serum starvation. For PKA (cAMP-dependent kinase) activation, we used Forskolin treatment for 1 h (FSK, 1 µM).

Reverse-Transcription Quantitative Real-Time PCR

RNA was extracted from fibroblasts via the RNeasy kit (QIAGEN), and first-strand cDNA was synthesized via the GeneAmp RNA PCR Core kit (Applied Biosystems) with random hexamer primers. Quantitative real-time PCR was carried out with the GoTaq qPCR master mix (Promega) in a Realplex 2 Mastercycler (Eppendorf) with *SMO*, *GLI1*, and *PTCH1* primers and primers for two house-keeping genes, *GUSB* and *HPRT* (Table S2). *SMO*, *GLI1*, and *PTCH1* expression data performed in triplicate were normalized to *GUSB* and *HPRT* mRNA expression data. Data were analyzed with the $2^{-\Delta\Delta Ct}$ method. Data are presented as relative expression ± SEM. **p < 0.05; ***p < 0.001 (Kolmogorov-Smirnov test).

Western Blot

Protein was extracted from fibroblasts with radioimmunoprecipitation assay buffer (RIPA buffer) containing Protease Inhibitor Cocktail (Roche). 50 µg of protein was separated by 10% SDS-PAGE and probed with rabbit anti-*GLI3* AF3690 antibody (Research and Diagnostic Systems, 1:500) followed by HRP-conjugated secondary antibody and ECL-Prime detection (Amersham). An antibody against glyceraldehyde 3-phosphate dehydrogenase (GAPDH; Abcam; ab9458) was used as a loading control. Densitometry with Bio-Rad Image Lab software was used for protein quantification.

Immunofluorescent Analysis

Fibroblasts were fixed in 4% paraformaldehyde (PFA) or in ice-cold methanol, permeabilized with 0.2% Triton X-100, and incubated in 3% BSA, 0.1% Tween20 before incubation with primary antibodies at 4°C overnight and subsequent incubation with secondary antibodies for 30 min at room temperature. DNA was stained with DAPI. Confocal images were taken on a Zeiss LSM 700 microscope. Images were analyzed with ImageJ. All experiments were performed in triplicate; four fields were acquired per condition, and there was an average of 15 cells per field. Cilia frequency was calculated from PC counts divided by nuclei counts. PC length was measured after 3D reconstruction of PC via Imaris software (Bitplane AG), which allowed for length assessment irrespective of the angle of orientation. To characterize *SMO* and *GLI2* trafficking to the PC, we measured the percentage of cells with *SMO* within the PC and those with an enrichment of *GLI2*

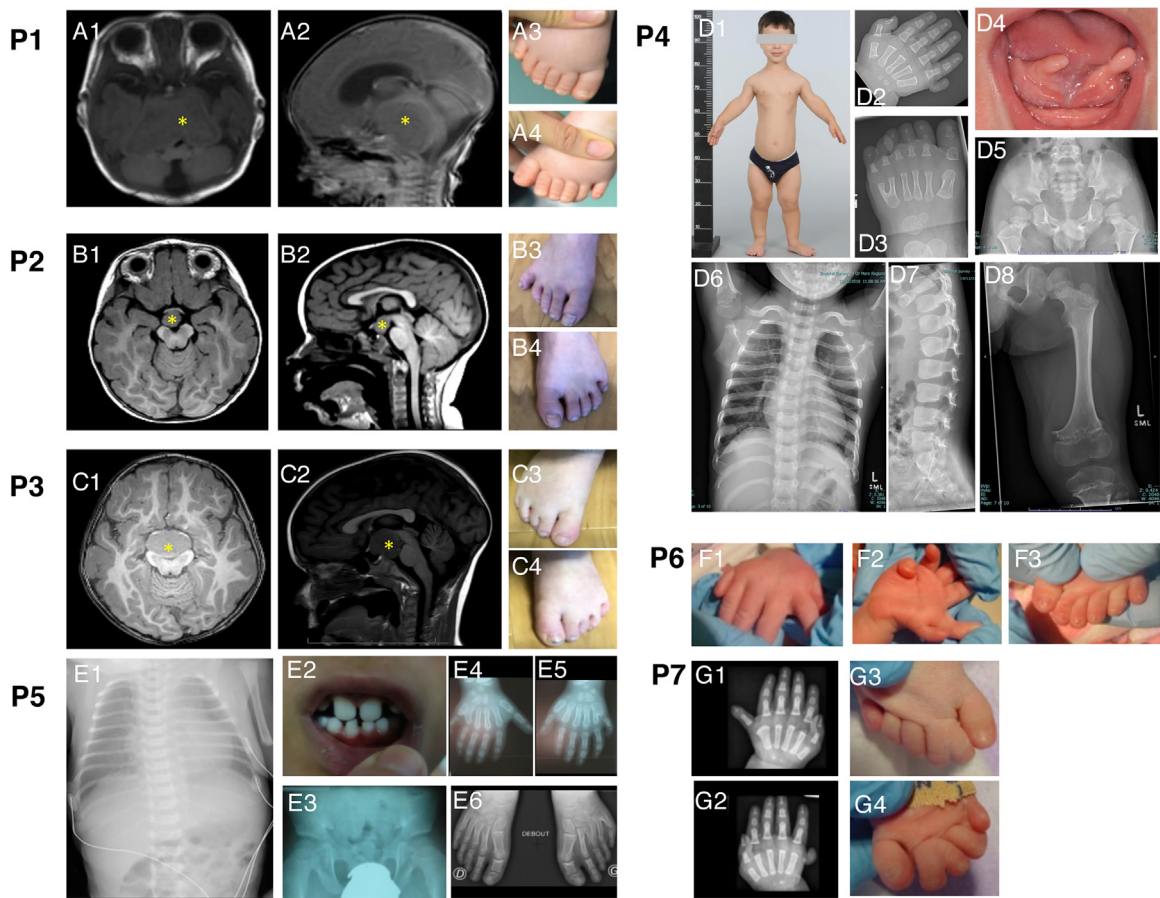


Figure 1. Clinical Features of Affected Individuals

Brain MRI sections on axial T1 (A1, B1, and C1) and sagittal T1 (A2, B2, and C2) show hypothalamic hamartoma in P1–P3 (yellow stars). P1 had postaxial polydactyly of lower limbs (A3 and A4). P2 and P3 had bilateral postaxial polydactyly of lower limbs with scars on the fifth digits after surgical removal of the sixth digits (B3 and B4). P3 also had syndactyly of the second and third digits of both feet (C3 and C4). P4 had short-limbed disproportionate short stature, with a narrow thoracic cage (D1), postaxial polydactyly with hypoplasia of middle and distal phalanges and Y-shaped metatarsal (D2 and D3), paired sublingual fleshy appendages surgically resected in infancy (D4), trident pelvis with thick pubic and ischial bones (D5), short ribs with metaphyseal cupping (D6), ovoid vertebral bodies (D7), and short long bones with metaphyseal lucency and sclerosis (D8). P5 presented with complete AVSD (not shown), a long and narrow thorax (E1), oligodontia (E2), a trident acetabular roof (E3), postaxial polydactyly of both hands (E4 and E5), and a Y-shaped metatarsal of the left foot (E6). P6 and P7 had AVSD (not shown), postaxial polydactyly of all four limbs (F1–G4), and two-thirds syndactyly of both feet (G3 and G4).

at the PC tip after SAG or rhSHH treatment. All antibodies are listed in Table S3.

Statistical Analysis

Results are presented as means of at least $n = 3$ independent experiments. Statistical analyses on pooled data were performed with the GraphPad Prism software via Kruskal-Wallis tests, Kolmogorov-Smirnov tests, or Fisher's exact tests.

Results

P1, a male, is the only child of non-consanguineous parents originating from France (F1-II:1). At birth, he presented with postaxial polydactyly of all four limbs, hypothalamic hamartoma, gelastic epilepsy, and Hirschsprung disease (HSCR [MIM: 142623]) (Figure 1 and Tables 1 and S1). PHS was suspected, and high-throughput sequencing of a diagnostic panel of genes causing human ciliopathies

or disorders of Hh-signal transduction including *GLI3* [MIM: 146510] identified no mutation. Whole-exome sequencing (WES) in trio revealed two heterozygous variants in *SMO* (GenBank: NM_005631.4): a missense c.781C>T (p.Arg261Cys) and a nonsense c.1339G>T (p.Glu447*) mutation, each inherited from one parent (Figure 2 and Table 2). The nonsense variant falls in exon 7 of 12 total and is therefore presumed to lead to loss of function via nonsense-mediated mRNA decay (NMD). Accordingly, quantitative real-time PCR on mRNA extracted from fibroblasts from P1 showed *SMO* expression decreased to 50% in comparison to age-matched controls (Figure 3A), and subsequent cDNA sequencing confirmed that almost all remaining *SMO* mRNAs carried the missense allele (Figure 3B). 3D modeling of the active G_i-coupled hSMO crystal structure (PDB: 6OT0)¹² showed that the Arg261 residue is located in the intracellular loop 1 (ICL1), which has been proposed to be crucial for

Table 1. Clinical Description of Individuals with Bi-allelic Variants in *SMO*

Affected Individuals	F1-II:1 (P1)	F2-II:1 (P2)	F2-II:2 (P3)	F3-II:1 (P4)	F4-II:4 (P5)	F5-II:2 (P6)	F5-II:3 (P7)
Gender	male	male	male	male	male	male	female
Age at last examination	3 years	7 years	4 years	5 years	8 years	deceased at 3 months	8 years
Psychomotor development	normal	normal	normal	mild delay	normal	NR	normal
Gelastic epilepsy	+	+	+	-	-	-	-
Hypothalamic hamartoma	+	+	+	-	-	NA	NA
Microcephaly	-	+	-	-	-	-	-
Dysmorphic facial features	+	+	+	+	-	-	-
Chest and rib abnormalities	-	-	-	+	moderate	-	-
Postaxial polydactyly	+	+	+	+	+	+	+
Syndactyly	-	5/6	2/3	5/6	-	2/3	2/3
Cardiac defect	-	-	-	-	+	+	+
Hirschsprung disease	+	-	-	-	-	-	-

Abbreviations: NA, not available; NR, not relevant.

SMO interaction with the G_{αi} protein, a direct downstream effector of SMO (Figures 3C and 3D).¹³ Structural comparison of active G_i-coupled hSMO and inactive hSMO (PDB: 5L7D)¹⁴ showed different conformations of Arg261, suggesting its involvement in the activation of SMO (Figure 3E). In addition, the substitution of Arg with Cys at amino acid 261 is predicted to modify the distance of the hydrogen bond between this residue and the Tyr262 backbone (Figure 3F), potentially affecting the stability of the protein.

WES analysis of other individuals with a PHS-like phenotype without *GLI3* variants led to the identification of bi-allelic variants in *SMO* in two affected siblings in family F2 [F2-II:1 (P2) and F2-II:2 (P3)]; these variants were inherited from their heterozygous parents. Both siblings presented with hypothalamic hamartoma, gelastic epilepsy, and postaxial polydactyly. In addition, P2 had microcephaly (Figure 1 and Tables 1 and S1) as previously reported.¹⁵ The paternally inherited variant, c.2291_2292del-AG, is located in the last exon of *SMO* and thus predicted to escape NMD and lead to a truncated protein, p.Gln764Argfs*52. The maternally inherited variant was suspected by WES to be a deletion of at least 29 Kb encompassing exon 1 of *SMO* and exons 2–8 of *TSPAN33*. In an attempt to confirm the deletion and define the break points, we used targeted resequencing of genomic DNA from P2 to capture a region of 153 Kb covering the deleted interval (Figure 2). This analysis and subsequent Sanger sequencing with breakpoint-flanking primers indicated that the deletion breakpoints are 62 Kb apart (chr7:g.128778292_128840690del), encompassing exon 1 of *SMO* and all exons of *TSPAN33* (Figure S1). Interestingly, both break points map to two short interspersed nuclear elements (SINEs) of the same Alu family: AluSx and AluSz repeats (Figure 2). This suggests non-homologous allelic recombination as the deletion mechanism. No *TSPAN33*

variant was identified in the hemizygous allele of the affected siblings. Reverse-transcription quantitative real-time PCR on mRNA extracted from fibroblasts of the siblings revealed a decrease of *SMO* expression by 50% compared to controls (Figure 3A). cDNA sequencing identified the mRNA harboring the 2 bp deletion that had escaped NMD (Figure 3B) and that is predicted to lead to a truncated protein lacking a part of the C-terminal cytoplasmic tail of SMO required for SMO ciliary accumulation and activation.^{16,17} In particular, this highly evolutionarily conserved region contains two serine residues (Ser771 and Ser785) corresponding to Ser777 and Ser791 in mouse Smo (mSmo) (Figures 3C and S2); these residues constitute two out of six phosphorylation sites essential for controlling SMO activation and ciliary localization.¹⁶

We also identified *SMO* bi-allelic variants in four additional individuals who had syndromic postaxial polydactyly and are from three different families. In family 3, the affected male [(F3-II:1 (P4)] had been diagnosed with Jeune asphyxiating thoracic dysplasia (JATD [MIM: 208500]). He presented with bilateral, symmetrical sublingual soft-tissue appendages; disproportionate short stature; short ribs; a trident appearance of the pelvis; short long bones; and postaxial polydactyly of all four limbs (Figure 1 and Tables 1 and S1). By using trio WES, we identified that he was homozygous for a *SMO* variant, c.1285A>T (p.Ile429Phe), which was inherited from both of his parents. This variant is predicted *in silico* to be deleterious for the function of the protein (Table 2) but is also predicted to affect splicing by reinforcing a cryptic acceptor splice site located 26 bp downstream of the canonical one. Quantification of *SMO* expression showed a decrease of 60% in P4's fibroblasts compared to control cells (Figure 3A). cDNA sequencing confirmed a partial splicing defect (p.Gly422Glufs*9) that resulted in the skipping of the first 26 bp of exon 7 (Figure 3B) and led to a frameshift and a premature stop

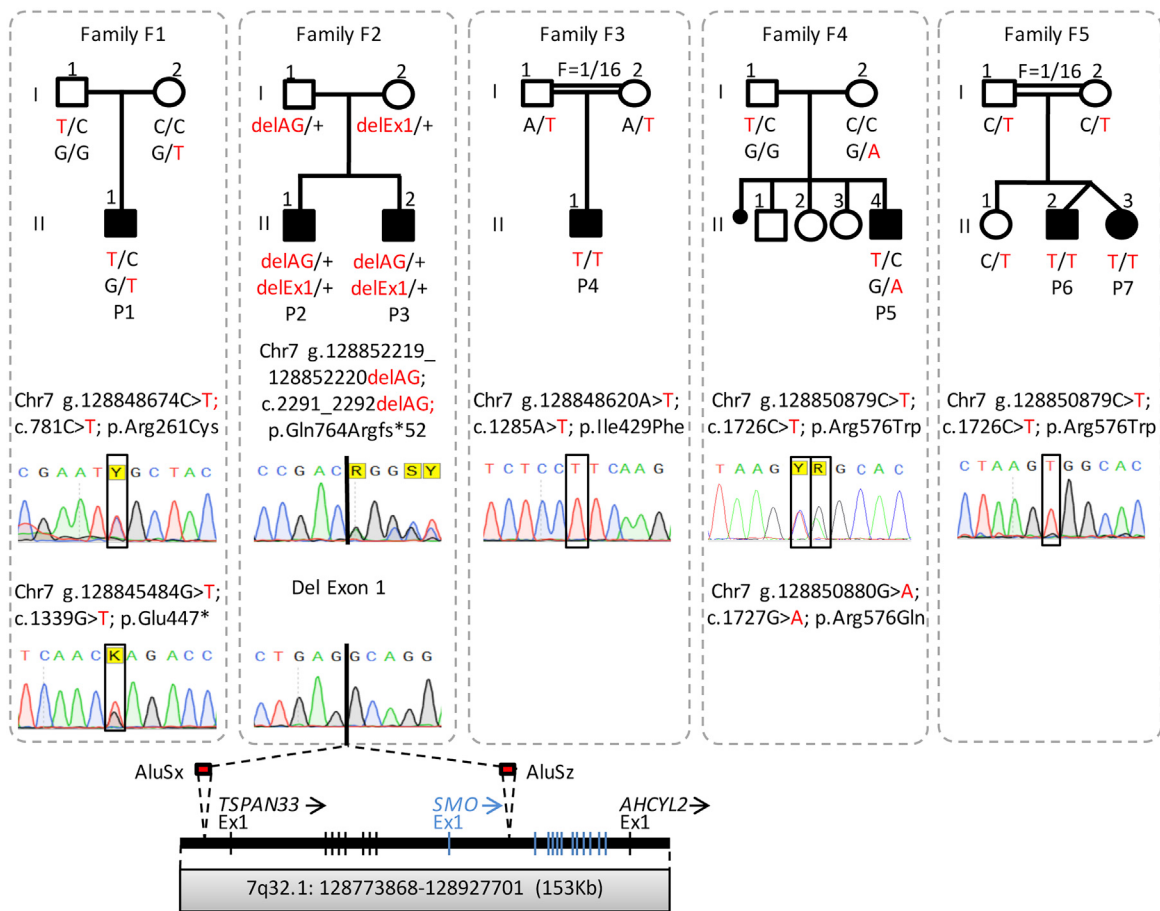


Figure 2. Pedigrees of the Five Families Carrying *SMO* Bi-allelic Variations

SMO variants are reported on the basis of Human Genome Assembly GRCh37 (hg19), and the *SMO* reference sequence used was GenBank: NM_005631.4. *SMO* variants were confirmed by Sanger sequencing on genomic DNA extracted from peripheral blood samples or fibroblasts of affected individuals and their parents. All variants segregated as expected from an autosomal recessive mode of inheritance in all available family members. In individual P2 from family F2, a large heterozygous deletion encompassing *SMO* and *TSPAN33* inherited from the mother was identified by targeted sequencing of a region of 153 Kb (7q32.1: 128773868–128927701). DNA breakpoints mapped to AluSx and AluSz repeats (red boxes) located at the borders of the deleted region (chr7:g.128778292_128840690del).

codon. This abnormal transcript partially escapes NMD and might be translated to a truncated SMO that lacks the TM5–6 and C-terminal tail and is thus predicted to be unstable or inactive. Ile429, which is located in the intracellular loop 3 (ICL3; Figures 3C and 3D), is involved in SMO interaction with the $\alpha 5$ helix of the $\text{G}\alpha_i$ protein required for SMO-mediated signal transduction.¹² In family F4, the affected child [F4-II:4 (P5)] presented with characteristic features of EVC syndrome, another short-rib thoracic dysplasia (SRTD); features included multiple gingival frenulae with dysplastic teeth (small, conical), complete atrioventricular septal defect (AVSD [MIM: 606215]), postaxial polydactyly of the upper limbs with Y-shaped metaphysis, a narrow chest, and a trident-shaped pelvis but normal stature (Figure 1 and Tables 1 and S1). Analysis of trio WES led to the identification of *SMO* compound heterozygous variants affecting the same amino acid residue: c.1727G>A (p.Arg576Gln) and c.1726C>T (p.Arg576Trp). Finally, a *SMO* homozygous missense variant also involving Arg576, c.1726C>T

(p.Arg576Trp), was detected in a fifth family with two affected siblings [F5-II:2 (P6) and F5-II:3 (P7)] born to consanguineous parents and presenting complete (P6) or partial (P7) AVSD and postaxial polydactyly of all four limbs (Figure 1 and Tables 1 and S1). In fibroblasts from P6 and P7, the expression of *SMO* remained in the normal range compared to that of controls, indicating stability of the mutated mRNAs (Figure 3A), and sequencing of fibroblast-derived cDNA confirmed the presence of the variant (Figure 3B). All three missense variants reported here are predicted deleterious *in silico* by PolyPhen2, SIFT, and CADD (Table 2). Finally, Arg576 is located in the C-terminal cytoplasmic tail required for SMO activation, as shown by previous studies indicating that mutagenesis of the corresponding Arg580 in mSmoo resulted in severe loss of mSmoo activity.¹⁸

To first analyze PC assembly in cells of individuals harboring bi-allelic *SMO* variants, we induced ciliogenesis by using serum-starvation-mediated cell-cycle arrest in confluent fibroblasts from five affected individuals

Table 2. Summary of Identified SMO Variations

Individuals	Genomic Position (hg19)	cDNA (GenBank: NM_005631.4)	Protein	gnomADv2.1.1	CADD v4.1	SIFT	PolyPhen2	Inheritance
P1-II:1	Chr7:g.128845484C>T	c.781C>T	p.Arg261Cys	1/121411/0	34	deleterious (0.01)	disease causing (1)	comp. htz.
	Chr7:g.128848674G>T	c.1339G>T	p.Glu447*	0	44	NA	NA	comp. htz.
P2-II:1 and 2	Chr7:g.128778292_128840690del	NA	NA	NA	NA	NA	NA	comp. htz.
	Chr7:g.128852219_128852220del	c.2291_2292del	p.Gln764Argfs*52	0	NA	NA	NA	comp. htz.
P3-II:1	Chr7:g.128848620A>T	c.1285A>T	p.Ile429Phe	0	27.3	deleterious (0.03)	disease causing (1)	htz.
P4-II:4	Chr7:g.128850880G>A	c.1727G>A	p.Arg576Gln	1/251186/0	33	deleterious (0)	disease causing (1)	comp. htz.
	Chr7:g.128850879C>T	c.1726C>T	p.Arg576Ter	2/121410/0	33	deleterious (0)	disease causing (1)	comp. htz.
P5-II:2 and 3	Chr7:g.128850879C>T	c.1726C>T	p.Arg576Ter	2/121410/0	33	deleterious (0)	disease causing (1)	htz.

Abbreviations: Comp. htz., compound heterozygous; htz., homozygous; CADD, combined annotation-dependent depletion; gnomAD data are presented as allele count/allele number/number of htzs.

(P1–P4 and P6) and two control individuals (C1 and C2) and visualized PC by immunostaining with antibodies raised against acetylated alpha tubulin and pericentrin. We found normal PC number, size, and shape in cells from all affected individuals compared to controls (Figures 4A–4C). These results are in accordance with previous observations in animal models where Smo is not required for normal ciliogenesis. We next tested the transduction of the Hh pathway in P1–P4, P6, and P7 cells stimulated by the addition of recombinant human SHH (rhSHH) or smoothened agonist (SAG) followed by quantification of the expression of two Hh target genes, *GLI1* and *PTCH1*. In contrast to findings in control cells, neither *GLI1* nor *PTCH1* expression was induced in cells from affected individuals, indicating a severe alteration of Hh pathway transduction (Figure 4D). These results suggest a loss-of-function mechanism of the identified *SMO* variants in the affected individuals.

We next analyzed SMO trafficking to the PC in response to rhSHH stimulation in cells derived from affected individuals. In control cells, SMO is enriched within the PC in response to rhSHH treatment. In cells from affected individuals, SMO is undetectable within the PC in three cases (P1, P2, and P3; Figures 4E and 4F), suggesting early destabilization or altered trafficking of mutated SMO and supporting the hypothesis of a loss-of-function mechanism. In the remaining two affected individuals (P4 and P6), SMO is only partially translocated into the PC, as evidenced by the fact that the percentage of SMO-positive PC appears to be significantly diminished as compared to that in controls. The transduction of the Hh signal remains as severely depleted as in P1–P3, suggesting that although it is partly translocated into the PC, SMO is not activated. Similarly, in cellular models, ciliary accumulation without activation of SMO is not sufficient for Hh-signal transduction.¹⁹ Taken together, these results suggest that the identified SMO variants alter the Hh pathway via the instability of the protein, altered SMO trafficking to the PC, or absence of SMO activation within the PC.

GLIs are the major transcriptional effectors of the Hh pathway, and GLI2 and GLI3 act as bifunctional transcription factors that contain both an N-terminal repression domain and a C-terminal transcriptional activation domain. When the pathway is off, GLI2 and GLI3 are targeted to the proteasome in a PC-dependent manner that promotes the processing of short forms with transcriptional repressor activity (GLI^R); GLI3^R acts as the primary repressor. We thus analyzed GLI3 processing in unstimulated cells from affected individuals and found an unaltered GLI3^{FL}:GLI3^R ratio compared to that of control cells (Figures 5A and 5B); this finding is in accordance with the SMO-independent processing of GLI transcription factors when the pathway is off. When the pathway is on, GLI2 mediates the bulk of Hh activation, whereas GLI3 processing is inhibited. We thus analyzed GLI3 processing in cells from affected individuals after activation by SAG and found no significant difference in the GLI3^{FL}

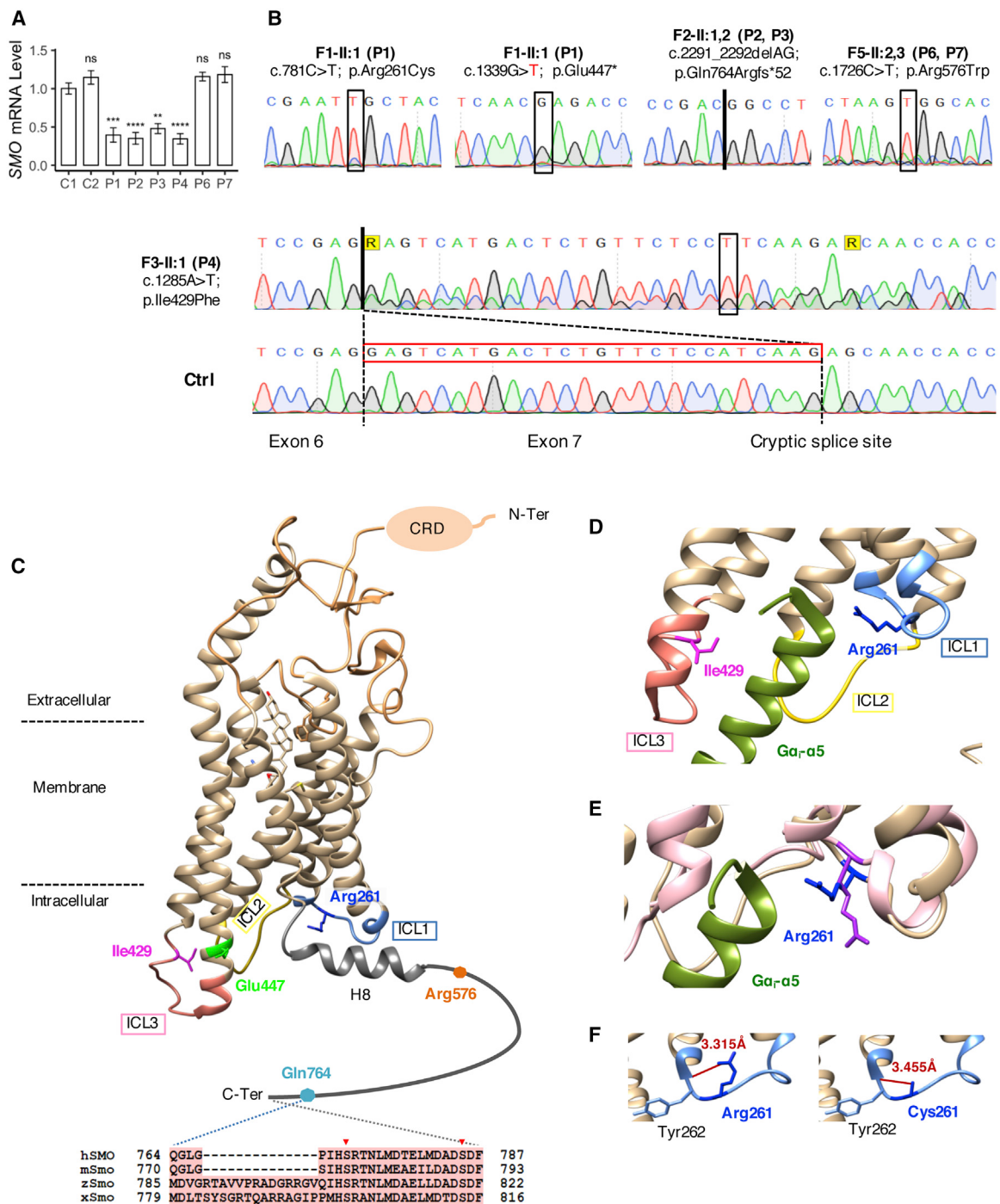


Figure 3. Effects of SMO Variants on the Expression of SMO

(A) Quantification of SMO transcripts by quantitative real-time PCR showed an expression decreased by 50%–60% in P1–P4 compared to controls and an expression similar to controls in P6 and P7. Quantitative real-time PCR was performed with primers specific to SMO transcript on mRNA extracted from fibroblasts of affected individuals and two unrelated age-matched controls. Data from three independent experiments were normalized to *GUSB* and *HPRT* mRNA levels, analyzed with the $2^{-\Delta\Delta Ct}$ method, and presented as mean values \pm SEM. ** $p < 0.05$; *** $p < 0.001$ (Kruskal-Wallis test).

(B) Sanger sequencing on cDNA from P1–P4, P6, and P7. Missense variants are indicated in black boxes, and deletion or splicing variants are indicated by black lines. For P4, both canonical and cryptic splice sites are indicated, and the red box highlights the skipped region. (C–F) 3D modeling of the identified variants on the active G_i -coupled human SMO crystal structure (PDB: 6OT0). The Arg261 and Ile429 residues are located at the ICL1 and ICL3, respectively (C and D). The predicted truncated protein terminating at the Glu447 residue lacks all the TM6, TM7, ECL3, and the C-terminal intracellular tail of SMO (C). The Arg576 in the C-terminal tail of SMO corresponding to Arg580 in mSmo is a critical residue required for downstream signaling (C). c.2291_2292delAG causes a frameshift leading to a truncated SMO lacking the distal C-terminal tail. The distal C-terminal tail is highly conserved throughout evolution and comprises two

(legend continued on next page)

:GLI3^R ratio between unstimulated and stimulated cells, suggesting abnormal inhibition of GLI3 processing in response to activation of the Hh pathway. In control cells, GLI3^R appeared to be decreased in response to Hh stimulation, leading to an increased GLI3^{FL}:GLI3^R ratio that was not statistically significant (Figures 5A and 5B).

We next analyzed the ciliary trafficking of GLI2, the principal mediator of Hh-dependent transcriptional activation, and found accumulation at PC tips in cells from affected individuals independently of rhSHH treatment (Figures 5C and 5D). In fact, the number of PC with enrichment of GLI2 at the tip in either unstimulated or stimulated cells from affected individuals was approximately the same as that in control cells stimulated by rhSHH treatment (Figure 5C). This result shows constitutive GLI2 localization to the PC when SMO is defective and is in agreement with animal models showing that the nuclear trafficking of GLI2 is regulated by the Hh-dependent accumulation of activated SMO within the PC. In particular, these findings are similar to those obtained in *Smo*^{-/-} mouse embryonic fibroblasts (MEFs) where both GLI2 and its inhibitor partner, SUFU, are also enriched at PC tips independently of rhSHH stimulation.²⁰

The cAMP-activated kinase PKA is one of the key players in the Hh pathway, and its activity is correlated with the amount of ciliary cAMP. In the absence of Hh signal, PKA phosphorylates GLI, leading to the proteolytic processing of GLI^{FL} into GLI^R. When the pathway is on, PC accumulation of activated SMO results in the inhibition of PKA and the dissociation of GLI from their inhibitory factor, SUFU, allowing GLI activation and translocation into the nucleus to activate Hh target genes. Importantly, in addition to its role in GLI processing, PKA restrains the activation of GLI2 by controlling GLI-SUFU association and dissociation as well as trafficking within the PC when the pathway is off.²¹ We thus analyzed the subcellular localization of PKA by immunostaining. In cells from all control and affected individuals, PKA accumulates at the base of the PC (Figure S3). After treatment with forskolin (FSK), a pharmacological agent that raises intracellular cAMP concentration, the PKA catalytic subunit is dispersed in cells from all control and affected individuals (Figure S3), indicating a normal PKA response to activating signal. In addition, we found that FSK treatment reverses rhSHH-independent GLI2 accumulation at the PC tip of cells from affected individuals, as evidenced by the fact that GLI2 was not detected at the PC tip in all cells analyzed (100 cells per experiment; Figure 5D). Whether PKA is the unique mediator of GLI2 accumulation remains to be determined because GLI2 also disappears from the PC tip after FSK treatment in *Pka*^{-/-} mouse cells.²¹

Discussion

Here, we report bi-allelic loss-of-function mutations of *SMO* in individuals with a wide range of malformations. All variants we identified are either extremely rare and not observed in a homozygous state (<10⁻⁵ alleles) or not reported in GnomAD, and all missense variants are predicted to alter SMO function (Table 2). Of those tested, each genotype leads to severely altered Hh-signal transduction with the absence of activation of Hh target genes after Hh stimulation. This depleted Hh-signal transduction is associated with reduced *SMO* expression or an altered SMO translocation to the PC in response to Hh stimulation for mutations p.Arg261Cys, p.Glu447*, and p.Gln764Argfs*52and for the 62 Kb deletion encompassing exon 1 of *SMO*. For variants p.Arg576Trp and p.Ile429-Phe, the mutant proteins are partially translocated to the PC in response to Hh stimulation but are unable to transduce the Hh signal, in accordance with their location in domains required for SMO activation (intracellular C-terminal domain)^{16–18,22} or SMO coupling to G-protein (ICL1, ICL3), both of which are required for full activation of Hh signaling.^{12,13,23,24}

We also examined GLI2 and GLI3 regulation in cells from affected individuals. Concerning GLI3, the major repressor when the pathway is off, we observed an unaltered GLI3^{FL}:GLI3^R ratio, indicating normal proteolytic processing. This ratio remained unchanged in cells from affected individuals after Hh pathway stimulation, in accordance with previous findings *in vitro* that *Smo* knockdown or inactivation prevented Hh-mediated inhibition of Gli3 processing.²⁵ However, the apparent increase in the GLI3^{FL}:GLI3^R ratio after stimulation in control cells remained statistically non-significant. Thus, we cannot draw conclusions about the potential involvement of GLI3 in the pathological mechanisms associated with SMO mutations in humans.

Concerning the ciliary trafficking of GLI2, the principal mediator of Hh-dependent transcriptional activation, GLI2 accumulates at the PC tip in cells from affected individuals independently of Hh stimulation. Thus, altered Hh signaling in cells from affected individuals is not due to an altered entry of GLI2 into the PC but might be due to an abnormal exit of GLI2 from the PC. This is caused by the absence of active SMO in the PC; this absence should lead to SUFU-GLI complex dissociation and subsequent GLI activation and translocation into the nucleus to activate Hh target genes. Furthermore, this GLI2 accumulation at the PC tip in cells from affected individuals is Hh-independent and thus might be due to an abnormal regulation of basal trafficking of GLI2, which normally shuttles in and out of the PC independently of

phosphorylation sites (Ser771 and Ser785, red arrowheads in the aligned sequences of human [h], mouse [m], zebrafish [z], and *Xenopus* [x] SMO proteins). Structural comparison of G_i-coupled hSMO and inactive hSMO (PDB: 5L7D) showed different conformations of the Arg261 (blue for active and purple for inactive conformations) (E). The substitution of Arg with Cys at amino acid 261 modified the distance of the hydrogen bond (in red) between this residue and the Tyr262 (F).

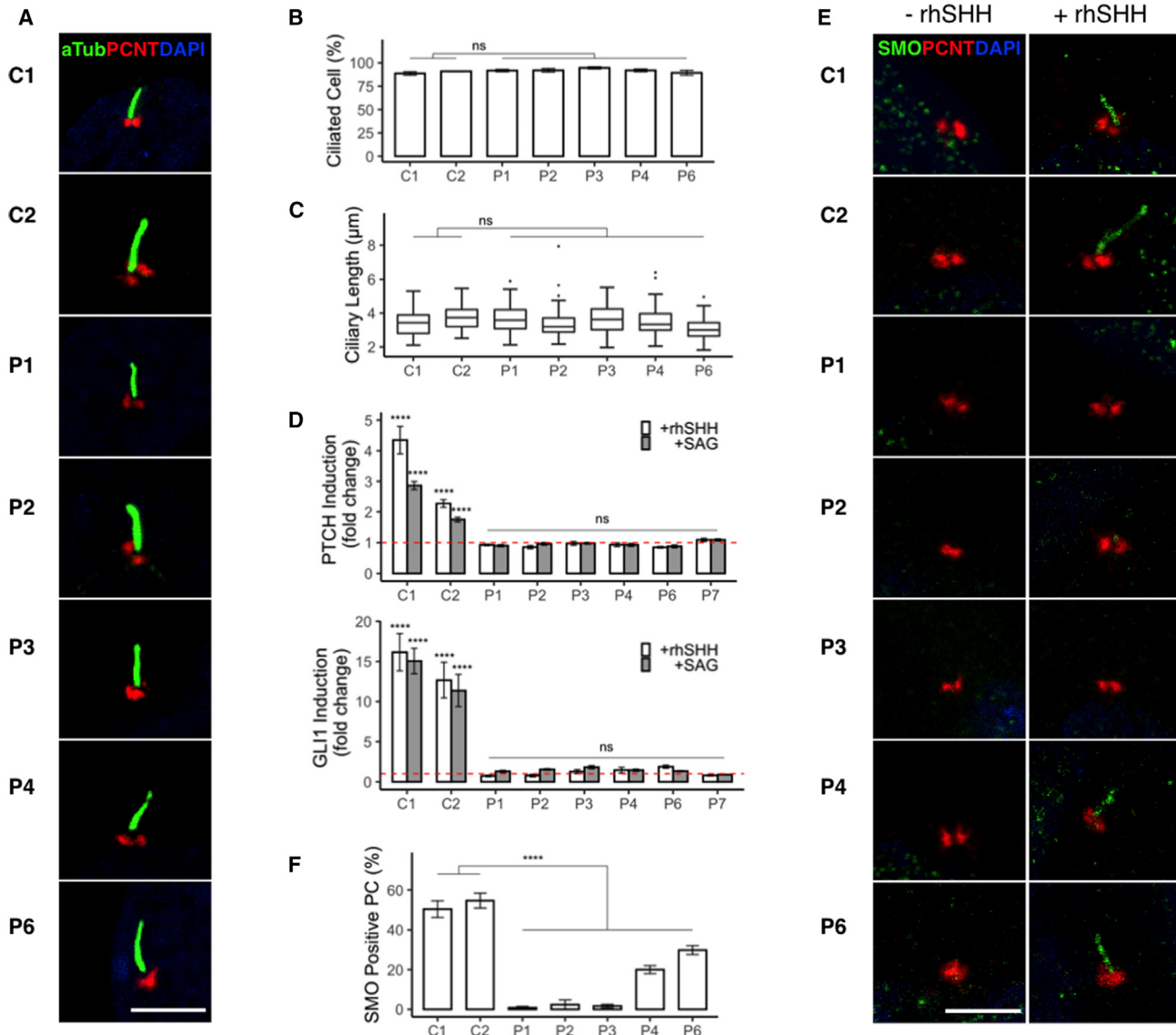


Figure 4. Normal Ciliogenesis but Altered Hh Signaling Transduction and SMO Trafficking in Cells from Affected Individuals

(A and B) Representative images and quantification of ciliogenesis in cells from controls and affected individuals. PC protruded from most cells of controls and affected individuals (~100 cells analyzed in three independent experiments). We calculated the percentage of ciliated cells by dividing PC counts by nuclei counts. Data are summarized in bar charts (mean values \pm SEM) in (B).

(C) Measurement of PC length after 3D reconstruction showed normal PC length in cells from affected individuals as compared to those from controls. Data represented in box and whisker plots are from three independent experiments (~100 cells analyzed per experiment).

(D) Assessment of the Hh-signal transduction by quantification of the induction of two Hh target genes *GLI1* and *PTCH1* on Hh-stimulated cells from controls and affected individuals. The expression of both genes is normally induced in controls, whereas no induction is found in any of the affected individuals tested. Values were presented as relative expression levels \pm SEM. The dashed red line indicates no induction of *GLI1* or *PTCH1* expression (ratio of stimulated versus unstimulated normalized expression = 1). ****p < 0.0001 (Kolmogorov-Smirnov test).

(E and F) Representative images (E) and quantification (F) of endogenous PC translocation of SMO in Hh-stimulated cells from control and affected individuals. Quantification was performed after stimulation (+rhSHH) or without stimulation (-rhSHH). Immunofluorescence analysis showed altered translocation of SMO to the PC in P1, P2, and P3 after Hh pathway induction as compared to controls. In P4 and P6, SMO appears translocated to the PC, whereas the percentage of positive SMO PC appears significantly diminished as compared to controls. Data from three independent experiments are summarized in bar charts (mean values \pm SEM). ****p < 0.0001 (Fisher's exact test). Scale bars represent 5 μm.

Hh stimulation.¹⁹ Our results suggest SMO involvement in regulating the basal ciliary trafficking of GLI2 when the pathway is off. Interestingly, GLI2 basal trafficking has been proposed to be regulated by PKA.²⁰ Thus, in this model, SMO could directly or indirectly regulate PKA,

which in turn could phosphorylate the GLI-SUFU complex to limit basal trafficking of GLI-SUFU within the PC.

All affected individuals shared postaxial polydactyly, a feature common to Hh signaling defects and to ciliopathies as the Hh pathway controls anterior to posterior

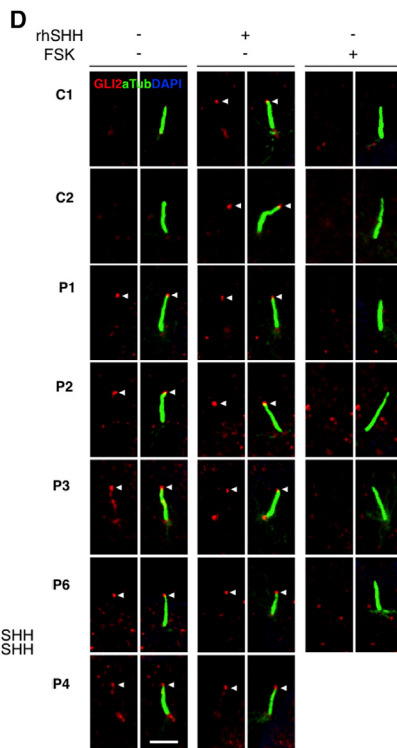
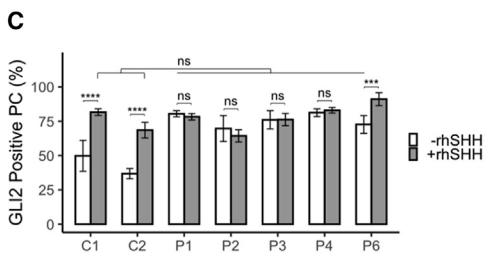
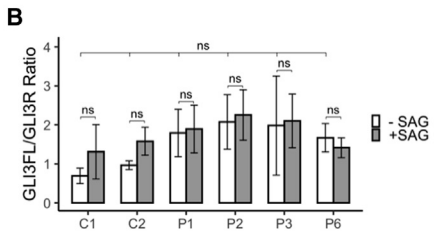
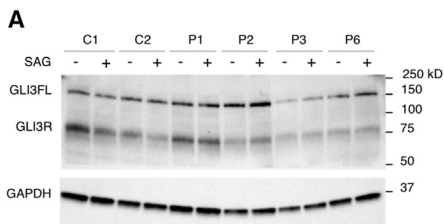


Figure 5. GLI2 and GLI3 Regulation in Cells of Individuals Harboring SMO Variants

(A and B) Image (A) and quantification (B) of western blot analysis on proteins extracted from cells of affected individuals and controls showed that the GLI3^{FL}:GLI3^R ratio remained unchanged between unstimulated and stimulated cells from affected individuals. In control cells, the GLI3^{FL}:GLI3^R ratio increased after SAG stimulation but without statistical significance. GAPDH was used as a loading control. Data are presented as mean values \pm SEM and statistical analysis was performed with a Kruskal-Wallis test.

(C and D) Representative images (C) and quantification (D) of GLI2-positive PC in cells from controls and affected individuals. In unstimulated control cells (-rhSHH), GLI2 is detectable at 30% of PC tips, whereas upon Hh stimulation (+rhSHH), GLI2 accumulates at the PC tips in 75% of cells. In cells of all affected individuals, GLI2 accumulates at the PC tips independently of Hh-stimulation (85%–90% of PC). Data from three independent experiments (~100 cells analyzed per experiment) are presented as mean values \pm SEM. ***p < 0.001, ****p < 0.0001 (Fisher's exact test). The scale bar represents 3 μ m.

growth and patterning of limb buds.^{26,27} In humans, mutations in each *GLI* have been associated with postaxial polydactyly. In particular, in individuals with PHS, the heterozygous mutations of *GLI3* lead to a truncated protein with constitutive repressor activity leading to an excess of GLI3^R relative to GLI3^A and subsequent pathway underactivation.²⁸ Here, we found that *SMO* mutations affect mostly GLI2 trafficking resulting in Hh pathway non-activation in response to Hh stimulation.

In addition to postaxial polydactyly, three affected individuals from families F4 and F5 presented with AVSD, a cardiac malformation previously associated with ciliopathies, including Bardet-Biedl (BBS [MIM: 209900]), Meckel (MKS [MIM: 249000]), and EVC syndromes, all of which are due to abnormal PC biogenesis and/or function.²⁹ The Hh pathway has long been shown to be crucial for cardiac septation as exemplified by the AVSD phenotype observed in *Shh*^{-/-} mice and conditional *Smo* mutants^{30,31} as well as in other mouse models of PC gene invalidation.^{29,32}

Two individuals from families F3 and F4 presented with radiographic features characteristic of SRTD in the context of JATD and EVC syndromes. Both syndromes belong to the group of skeletal ciliopathies in which mutations in genes encoding several components of the intraflagellar transport machinery necessary for building and maintaining the PC have been shown to be causal.^{33,34} Among these genes, mutations in *IFT80* cause JATD and short-rib polydactyly type III, secondary to abnormal ciliogenesis.^{35–37} Interestingly, treatment with the SMO agonist SAG, as well as GLI2 overactivation, was able to rescue the osteo-

genic deficiency of *IFT80*-silenced cells.³⁷ In addition, EVC can be caused by mutations in *EVC* and *EVC2*,^{38,39} encoding two proteins forming a ciliary transmembrane complex that interacts with SMO to transduce the Hh signal.^{40–42}

Concerning brain development, three individuals with a PHS-like phenotype discussed in the present report have hypothalamic hamartoma and gelastic epilepsy. Both are common features of PHS, which has been strongly associated with Hh signaling defects.⁴³ Hypothalamic hamartoma is also one of the clinical features of oral-facial-digital (OFD) syndrome types I and VI,^{44,45} two syndromic ciliopathies associated with PC dysfunction with subsequent Hh signaling reduction. Conditional deletion of *Smo* in mice showed its requirement for promoting tuberal hypothalamic neuronal identity and heterogeneity among distinct hypothalamic nuclei as well as for maintenance of tuberal hypothalamic progenitors in a proliferative state.⁴⁶ However, the mechanisms underlying hypothalamic hamartoma formation in the context of reduced Hh signaling are still unknown. Corman and collaborators recently proposed a mechanism by which a non-cell autonomous gain in Hh signaling activity in wild-type cells surrounding *Smo*-deleted cells (conditional deletion of *Smo* in Hh-responsive tuberal hypothalamic progenitors modeling mosaic *Smo* disruption) might cause growth of these benign tumors.⁴⁶ However, the affected individuals in our report harbor bi-allelic *SMO* mutations involving all cells and thus do not fit this model.

One individual (F2:II-1) presented with microcephaly, a feature that has also been reported in ciliopathies and is possibly associated with gyration defects. Interestingly, an appreciation of the involvement of PC and Hh signaling during neocortical development has recently emerged.^{47–50} For example, Wang et al. nicely showed that constitutively active Shh signaling via the *SmoM2* mutation in mice led to the expansion of neocortical progenitors and induced folding of the otherwise smooth neocortex, whereas the loss of Hh signaling decreased the number of neocortical progenitors and the size of the neocortex.⁵¹

HSCR is less commonly associated with anomalies of Hh-signal transduction or ciliopathies but is in accordance with the proposed functions of Hh signaling during gut development.^{52–54} In particular, targeted deletion of *Smo* in mice as well as *Gli1* or *Shh* overexpression leads to abnormal ENS development.^{55–57} HSCR has been reported in other ciliopathies or congenital anomalies of Hh-signal transduction, including BBS types 1 and 4–7,⁵⁸ JATD,⁵⁹ JBTS,⁶⁰ and PHS,⁶¹ although the predisposition to HSCR remains low in these disorders. In individual P1, HSCR could have been explained by an additional genetic event at the *RET* locus in which rare variations and frequent predisposing polymorphisms have been reported.^{62,63} Although no *RET* coding-sequence mutation was identified, P1 was heterozygous for the hypomorphic predisposing allele (rs2435357).⁶⁴ A larger cohort of individuals with ciliopathies or developmental anomalies of Hh signaling and HSCR could allow for elucidation of the genetic mechanisms leading to the HSCR trait, which might result from a mutational burden in PC genes and/or in genes encoding components of the RET signaling cascade as previously suggested in humans and zebrafish.⁵⁸ Along these lines, targeted sequencing of *GLI* in individuals with HSCR led to the identification of heterozygous rare variants predicted to be damaging yet inherited from unaffected parents.⁶⁵ Although these might not be sufficient alone to cause the phenotype, they could contribute to a higher mutational load in the RET and Hh signaling pathways as well as PC genes.^{65,66}

Finally, ocular anomalies were not reported in this study, whereas compound heterozygous missense *SMO* mutations were recently reported in a child with both anterior segment dysgenesis (congenital corneal opacity and cataract) and morning glory syndrome without other ciliopathy-like phenotypes.⁶⁷ In mice, conditional *Smo* deletion results in lens and corneal defects from embryonic day 14.5 (E14.5),⁶⁸ thus supporting the hypothesis that dysfunction of *SMO* is responsible for the ocular anomalies observed, although functional data concerning the pathogenicity of the variants reported by Zhang et al. is required.

Altogether, we report bi-allelic loss-of-function *SMO* mutations resulting in a broad spectrum of developmental anomalies affecting the brain (hypothalamic hamartoma and microcephaly), the heart (AVSD), the skeleton (post-axial polydactyly, narrow chest, and shortening of long

bones), and the gut (aganglionosis) in humans. Functional analysis in cells from affected individuals indicated severely impaired transduction of the Hh signaling pathway and altered PC trafficking of GLI2. Our results expand the range of human pathologies caused by *SMO* variations that, in addition to somatic mutations that cause cancer, now include germline mutations leading to a developmental disorder.

Supplemental Data

Supplemental Data can be found online at <https://doi.org/10.1016/j.ajhg.2020.04.010>.

Acknowledgments

We are grateful to the affected individuals and their families for their participation. We thank Marc Le Loch for help with targeted resequencing and Megan Cho for scientific networking. This work was supported by grants from the “Agence Nationale de la Recherche” (ANR) to S.T. (ANR-17-CE16-0003-01), MSDAvenir (DevoDecode project), and the “Fondation Maladies Rares” (HTS-RD-I20140502). T.L.L. is supported by the French Excellence Program of the French Embassy in Vietnam and the “Fondation pour la Recherche Médicale” (PhD program). The Imagine Institute is supported by state funding from the ANR under the “Investissements d’avenir” program (ANR-10-IAHU-01) and as part of the second “Investissements d’Avenir” program (ANR-17-RHUS-0002). The research conducted at the Murdoch Children’s Research Institute was supported by the Victorian Government’s Operational Infrastructure Support Program.

Declaration of Interests

The authors declare no competing interests.

Received: February 5, 2020

Accepted: April 8, 2020

Published: May 14, 2020

Web Resources

CADD, <https://cadd.gs.washington.edu>
Chimera, <https://www.cgl.ucsf.edu/chimera/>
Decipher, <https://decipher.sanger.ac.uk>
GenBank, <https://www.ncbi.nlm.nih.gov/genbank/>
GnomAD, <https://gnomad.broadinstitute.org/faq>
OMIM, <https://www.ncbi.nlm.nih.gov/omim>
PolyPhen-2, <http://genetics.bwh.harvard.edu/pph/>
Primer3plus, <https://primer3plus.com>
RCSB PDB, <http://www.rcsb.org/>
Sift, <https://sift.bii.a-star.edu.sg>
UCSC Genome Browser, <http://genome.ucsc.edu>

References

1. Huangfu, D., Liu, A., Rakeman, A.S., Murcia, N.S., Niswander, L., and Anderson, K.V. (2003). Hedgehog signalling in the mouse requires intraflagellar transport proteins. *Nature* **426**, 83–87.

2. Goetz, S.C., and Anderson, K.V. (2010). The primary cilium: a signalling centre during vertebrate development. *Nat. Rev. Genet.* *11*, 331–344.
3. Corbit, K.C., Shyer, A.E., Dowdle, W.E., Gaulden, J., Singla, V., Chen, M.-H., Chuang, P.-T., and Reiter, J.F. (2008). Kif3a constrains beta-catenin-dependent Wnt signalling through dual ciliary and non-ciliary mechanisms. *Nat. Cell Biol.* *10*, 70–76.
4. Rohatgi, R., Milenkovic, L., and Scott, M.P. (2007). Patched1 regulates hedgehog signaling at the primary cilium. *Science* *317*, 372–376.
5. Santos, N., and Reiter, J.F. (2014). A central region of Gli2 regulates its localization to the primary cilium and transcriptional activity. *J. Cell Sci.* *127*, 1500–1510.
6. Palencia-Campos, A., Ullah, A., Nevado, J., Yildirim, R., Unal, E., Ciorraga, M., Barruz, P., Chico, L., Piceci-Sparascio, F., Guida, V., et al. (2017). GLI1 inactivation is associated with developmental phenotypes overlapping with Ellis-van Creveld syndrome. *Hum. Mol. Genet.* *26*, 4556–4571.
7. França, M.M., Jorge, A.A.L., Carvalho, L.R.S., Costalonga, E.F., Vasques, G.A., Leite, C.C., Mendonca, B.B., and Arnhold, I.J.P. (2010). Novel heterozygous nonsense GLI2 mutations in patients with hypopituitarism and ectopic posterior pituitary lobe without holoprosencephaly. *J. Clin. Endocrinol. Metab.* *95*, E384–E391.
8. Xie, J., Murone, M., Luoh, S.M., Ryan, A., Gu, Q., Zhang, C., Bonifas, J.M., Lam, C.W., Hynes, M., Goddard, A., et al. (1998). Activating Smoothened mutations in sporadic basal-cell carcinoma. *Nature* *391*, 90–92.
9. Twigg, S.R.F., Hufnagel, R.B., Miller, K.A., Zhou, Y., McGowan, S.J., Taylor, J., Craft, J., Taylor, J.C., Santoro, S.L., Huang, T., et al. (2016). A recurrent mosaic mutation in SMO, encoding the hedgehog signal transducer smoothened, is the major cause of Curry-Jones syndrome. *Am. J. Hum. Genet.* *98*, 1256–1265.
10. Sobreira, N., Schietecatte, F., Valle, D., and Hamosh, A. (2015). GeneMatcher: a matching tool for connecting investigators with an interest in the same gene. *Hum. Mutat.* *36*, 928–930.
11. Rosain, J., Oleaga-Quintas, C., Deswarthe, C., Verdin, H., Marot, S., Syridou, G., Mansouri, M., Mahdaviani, S.A., Venegas-Montoya, E., Tsolia, M., et al. (2018). A variety of Alu-mediated copy number variations can underlie IL-12R β 1 deficiency. *J. Clin. Immunol.* *38*, 617–627.
12. Qi, X., Liu, H., Thompson, B., McDonald, J., Zhang, C., and Li, X. (2019). Cryo-EM structure of oxysterol-bound human Smoothened coupled to a heterotrimeric G β i. *Nature* *571*, 279–283.
13. Ogden, S.K., Fei, D.L., Schilling, N.S., Ahmed, Y.F., Hwa, J., and Robbins, D.J. (2008). G protein Galphai functions immediately downstream of Smoothened in Hedgehog signalling. *Nature* *456*, 967–970.
14. Byrne, E.F.X., Sircar, R., Miller, P.S., Hedger, G., Luchetti, G., Nachtergael, S., Tully, M.D., Mydock-McGrane, L., Covey, D.F., Rambo, R.P., et al. (2016). Structural basis of Smoothened regulation by its extracellular domains. *Nature* *535*, 517–522.
15. Rubino, S., Qian, J., Pinheiro-Neto, C.D., Kenning, T.J., and Adamo, M.A. (2018). A familial syndrome of hypothalamic hamartomas, polydactyly, and SMO mutations: a clinical report of 2 cases. *J. Neurosurg. Pediatr.* *23*, 98–103.
16. Chen, Y., Sasai, N., Ma, G., Yue, T., Jia, J., Briscoe, J., and Jiang, J. (2011). Sonic Hedgehog dependent phosphorylation by CK1 α and GRK2 is required for ciliary accumulation and activation of smoothened. *PLoS Biol.* *9*, e1001083.
17. Zhang, C., Williams, E.H., Guo, Y., Lum, L., and Beachy, P.A. (2004). Extensive phosphorylation of Smoothened in Hedgehog pathway activation. *Proc. Natl. Acad. Sci. USA* *101*, 17900–17907.
18. Varjosalo, M., Li, S.-P., and Taipale, J. (2006). Divergence of hedgehog signal transduction mechanism between *Drosophila* and mammals. *Dev. Cell* *10*, 177–186.
19. Kim, J., Kato, M., and Beachy, P.A. (2009). Gli2 trafficking links Hedgehog-dependent activation of Smoothened in the primary cilium to transcriptional activation in the nucleus. *Proc. Natl. Acad. Sci. USA* *106*, 21666–21671.
20. Tukachinsky, H., Lopez, L.V., and Salic, A. (2010). A mechanism for vertebrate Hedgehog signaling: recruitment to cilia and dissociation of SuFu-Gli protein complexes. *J. Cell Biol.* *191*, 415–428.
21. Tucson, M., He, M., and Anderson, K.V. (2011). Protein kinase A acts at the basal body of the primary cilium to prevent Gli2 activation and ventralization of the mouse neural tube. *Development* *138*, 4921–4930.
22. Jiang, K., Liu, Y., Fan, J., Zhang, J., Li, X.-A., Evers, B.M., Zhu, H., and Jia, J. (2016). PI(4)P Promotes Phosphorylation and Conformational Change of Smoothened through Interaction with Its C-terminal Tail. *PLoS Biol.* *14*, e1002375.
23. Nakano, Y., Nystedt, S., Shivedasani, A.A., Strutt, H., Thomas, C., and Ingham, P.W. (2004). Functional domains and subcellular distribution of the Hedgehog transducing protein Smoothened in *Drosophila*. *Mech. Dev.* *121*, 507–518.
24. Buck, F., Wang, W., Harder, S., Brathwaite, C., Bruhn, T.O., and Gershengorn, M.C. (2000). Juxtamembrane regions in the third intracellular loop of the thyrotropin-releasing hormone receptor type 1 are important for coupling to Gq. *Endocrinology* *141*, 3717–3722.
25. Wen, X., Lai, C.K., Evangelista, M., Hongo, J.-A., de Sauvage, F.J., and Scales, S.J. (2010). Kinetics of hedgehog-dependent full-length Gli3 accumulation in primary cilia and subsequent degradation. *Mol. Cell. Biol.* *30*, 1910–1922.
26. Verma, P.K., and El-Harouni, A.A. (2015). Review of literature: genes related to postaxial polydactyly. *Front. Pediatr.* *3*, 8.
27. Tickle, C., and Towers, M. (2017). Sonic Hedgehog signaling in limb development. *Front. Cell Dev. Biol.* *5*, 14.
28. Shin, S.H., Kogerman, P., Lindström, E., Toftgård, R., and Biesecker, L.G. (1999). GLI3 mutations in human disorders mimic *Drosophila* cubitus interruptus protein functions and localization. *Proc. Natl. Acad. Sci. USA* *96*, 2880–2884.
29. Burnicka-Turek, O., Steimle, J.D., Huang, W., Felker, L., Kamp, A., Kweon, J., Peterson, M., Reeves, R.H., Maslen, C.L., Gruber, P.J., et al. (2016). Cilia gene mutations cause atrioventricular septal defects by multiple mechanisms. *Hum. Mol. Genet.* *25*, 3011–3028.
30. Goddeeris, M.M., Rho, S., Petiet, A., Davenport, C.L., Johnson, G.A., Meyers, E.N., and Klingensmith, J. (2008). Intracardiac septation requires hedgehog-dependent cellular contributions from outside the heart. *Development* *135*, 1887–1895.
31. Lin, L., Bu, L., Cai, C.-L., Zhang, X., and Evans, S. (2006). Isl1 is upstream of sonic hedgehog in a pathway required for cardiac morphogenesis. *Dev. Biol.* *295*, 756–763.
32. Willaredt, M.A., Gorgas, K., Gardner, H.A.R., and Tucker, K.L. (2012). Multiple essential roles for primary cilia in heart development. *Cilia* *1*, 23.

33. Huber, C., and Cormier-Daire, V. (2012). Ciliary disorder of the skeleton. *Am. J. Med. Genet. C. Semin. Med. Genet.* **160C**, 165–174.
34. Schmidts, M., Hou, Y., Cortés, C.R., Mans, D.A., Huber, C., Boldt, K., Patel, M., van Reeuwijk, J., Plaza, J.-M., van Beersum, S.E.C., et al.; UK10K (2015). TCTEX1D2 mutations underlie Jeune asphyxiating thoracic dystrophy with impaired retrograde intraflagellar transport. *Nat. Commun.* **6**, 7074.
35. Beales, P.L., Bland, E., Tobin, J.L., Bacchelli, C., Tuysuz, B., Hill, J., Rix, S., Pearson, C.G., Kai, M., Hartley, J., et al. (2007). IFT80, which encodes a conserved intraflagellar transport protein, is mutated in Jeune asphyxiating thoracic dystrophy. *Nat. Genet.* **39**, 727–729.
36. Cavalcanti, D.P., Huber, C., Sang, K.-H.L.Q., Baujat, G., Collins, F., Delezoide, A.-L., Dagoneau, N., Le Merrer, M., Martinovic, J., Mello, M.F.S., et al. (2011). Mutation in IFT80 in a fetus with the phenotype of Verma-Naumoff provides molecular evidence for Jeune-Verma-Naumoff dysplasia spectrum. *J. Med. Genet.* **48**, 88–92.
37. Yang, S., and Wang, C. (2012). The intraflagellar transport protein IFT80 is required for cilia formation and osteogenesis. *Bone* **51**, 407–417.
38. Galdzicka, M., Patnala, S., Hirshman, M.G., Cai, J.-F., Nitowsky, H., Egeland, J.A., and Ginns, E.I. (2002). A new gene, EVC2, is mutated in Ellis-van Creveld syndrome. *Mol. Genet. Metab.* **77**, 291–295.
39. Ruiz-Perez, V.L., Tompson, S.W.J., Blair, H.J., Espinoza-Valdez, C., Lapunzina, P., Silva, E.O., Hamel, B., Gibbs, J.L., Young, I.D., Wright, M.J., and Goodship, J.A. (2003). Mutations in two nonhomologous genes in a head-to-head configuration cause Ellis-van Creveld syndrome. *Am. J. Hum. Genet.* **72**, 728–732.
40. Caparrós-Martín, J.A., Valencia, M., Reytor, E., Pacheco, M., Fernandez, M., Perez-Aytes, A., Gean, E., Lapunzina, P., Peters, H., Goodship, J.A., and Ruiz-Perez, V.L. (2013). The ciliary Evc/Evc2 complex interacts with Smo and controls Hedgehog pathway activity in chondrocytes by regulating Sufo/Gli3 dissociation and Gli3 trafficking in primary cilia. *Hum. Mol. Genet.* **22**, 124–139.
41. Dorn, K.V., Hughes, C.E., and Rohatgi, R. (2012). A Smoothened-Evc2 complex transduces the Hedgehog signal at primary cilia. *Dev. Cell* **23**, 823–835.
42. Yang, C., Chen, W., Chen, Y., and Jiang, J. (2012). Smoothened transduces Hedgehog signal by forming a complex with Evc/Evc2. *Cell Res.* **22**, 1593–1604.
43. Hildebrand, M.S., Griffin, N.G., Damiano, J.A., Cops, E.J., Burgess, R., Ozturk, E., Jones, N.C., Leventer, R.J., Freeman, J.L., Harvey, A.S., et al. (2016). Mutations of the Sonic Hedgehog pathway underlie hypothalamic hamartoma with gelastic epilepsy. *Am. J. Hum. Genet.* **99**, 423–429.
44. Poretti, A., Vitiello, G., Hennekam, R.C.M., Arrigoni, F., Bertini, E., Borgatti, R., Brancati, F., D'Arrigo, S., Faravelli, F., Giordano, L., et al. (2012). Delineation and diagnostic criteria of Oral-Facial-Digital Syndrome type VI. *Orphanet J. Rare Dis.* **7**, 4.
45. Azukizawa, T., Yamamoto, M., Narumiya, S., and Takano, T. (2013). Oral-facial-digital syndrome type 1 with hypothalamic hamartoma and Dandy-Walker malformation. *Pediatr. Neurol.* **48**, 329–332.
46. Corman, T.S., Bergendahl, S.E., and Epstein, D.J. (2018). Distinct temporal requirements for Sonic hedgehog signaling in development of the tuberal hypothalamus. *Development* **145**.
47. Thomas, S., Boutaud, L., Reilly, M.L., and Benmerah, A. (2019). Cilia in hereditary cerebral anomalies. *Biol. Cell* **111**, 217–231.
48. Park, S.M., Jang, H.J., and Lee, J.H. (2019). Roles of primary cilia in the developing brain. *Front. Cell. Neurosci.* **13**, 218.
49. Guo, J., Higginbotham, H., Li, J., Nichols, J., Hirt, J., Ghukasyan, V., and Anton, E.S. (2015). Developmental disruptions underlying brain abnormalities in ciliopathies. *Nat. Commun.* **6**, 7857.
50. Taverna, E., Götz, M., and Huttner, W.B. (2014). The cell biology of neurogenesis: toward an understanding of the development and evolution of the neocortex. *Annu. Rev. Cell Dev. Biol.* **30**, 465–502.
51. Wang, L., Hou, S., and Han, Y.-G. (2016). Hedgehog signaling promotes basal progenitor expansion and the growth and folding of the neocortex. *Nat. Neurosci.* **19**, 888–896.
52. Sukegawa, A., Narita, T., Kameda, T., Saitoh, K., Nohno, T., Iba, H., Yasugi, S., and Fukuda, K. (2000). The concentric structure of the developing gut is regulated by Sonic hedgehog derived from endodermal epithelium. *Development* **127**, 1971–1980.
53. Fu, M., Lui, V.C.H., Sham, M.H., Pachnis, V., and Tam, P.K.H. (2004). Sonic hedgehog regulates the proliferation, differentiation, and migration of enteric neural crest cells in gut. *J. Cell Biol.* **166**, 673–684.
54. Nagy, N., Barad, C., Graham, H.K., Hotta, R., Cheng, L.S., Fejszak, N., and Goldstein, A.M. (2016). Sonic hedgehog controls enteric nervous system development by patterning the extra-cellular matrix. *Development* **143**, 264–275.
55. Huang, H., Cotton, J.L., Wang, Y., Rajurkar, M., Zhu, L.J., Lewis, B.C., and Mao, J. (2013). Specific requirement of Gli transcription factors in Hedgehog-mediated intestinal development. *J. Biol. Chem.* **288**, 17589–17596.
56. Ramalho-Santos, M., Melton, D.A., and McMahon, A.P. (2000). Hedgehog signals regulate multiple aspects of gastrointestinal development. *Development* **127**, 2763–2772.
57. Yang, J.T., Liu, C.Z., Villavicencio, E.H., Yoon, J.W., Walterhouse, D., and Iannaccone, P.M. (1997). Expression of human GLI in mice results in failure to thrive, early death, and patchy Hirschsprung-like gastrointestinal dilatation. *Mol. Med.* **3**, 826–835.
58. de Pontual, L., Zaghloul, N.A., Thomas, S., Davis, E.E., McGaughey, D.M., Dollfus, H., Baumann, C., Bessling, S.L., Babarit, C., Pelet, A., et al. (2009). Epistasis between RET and BBS mutations modulates enteric innervation and causes syndromic Hirschsprung disease. *Proc. Natl. Acad. Sci. USA* **106**, 13921–13926.
59. Aurora, P., and Wallis, C.E. (1999). Jeune syndrome (asphyxiating thoracic dystrophy) associated with Hirschsprung disease. *Clin. Dysmorphol.* **8**, 259–263.
60. Ozuyrek, H., Kayacik, O.E., Gunor, O., and Karagoz, F. (2008). Rare association of Hirschsprung's disease and Joubert syndrome. *Eur. J. Pediatr.* **167**, 475–477.
61. Li, M.H., Eberhard, M., Mudd, P., Javaid, L., Zimmerman, R., Khalek, N., and Zackai, E.H. (2015). Total colonic aganglionosis and imperforate anus in a severely affected infant with Pallister-Hall syndrome. *Am. J. Med. Genet. A* **167A**, 617–620.
62. Edery, P., Lyonnet, S., Mulligan, L.M., Pelet, A., Dow, E., Abel, L., Holder, S., Nihoul-Fékété, C., Ponder, B.A., and Munnich, A. (1994). Mutations of the RET proto-oncogene in Hirschsprung's disease. *Nature* **367**, 378–380.

63. Amiel, J., Sproat-Emison, E., Garcia-Barcelo, M., Lantieri, F., Burzynski, G., Borrego, S., Pelet, A., Arnold, S., Miao, X., Griseri, P., et al.; Hirschsprung Disease Consortium (2008). Hirschsprung disease, associated syndromes and genetics: a review. *J. Med. Genet.* **45**, 1–14.
64. Emison, E.S., Garcia-Barcelo, M., Grice, E.A., Lantieri, F., Amiel, J., Burzynski, G., Fernandez, R.M., Hao, L., Kashuk, C., West, K., et al. (2010). Differential contributions of rare and common, coding and noncoding Ret mutations to multifactorial Hirschsprung disease liability. *Am. J. Hum. Genet.* **87**, 60–74.
65. Liu, J.A.-J., Lai, F.P.-L., Gui, H.-S., Sham, M.-H., Tam, P.K.-H., Garcia-Barcelo, M.-M., Hui, C.-C., and Ngan, E.S.-W. (2015). Identification of GLI mutations in patients with Hirschsprung disease that disrupt enteric nervous system development in mice. *Gastroenterology* **149**, 1837–1848.e5.
66. Young, H.M., Stamp, L.A., and Hofstra, R.M.W. (2015). Hirschsprung disease and activation of Hedgehog signaling via GLI1-3 mutations. *Gastroenterology* **149**, 1672–1675.
67. Zhang, J., Li, Y., Fan, Y., Wu, D., and Xu, J. (2019). Compound heterozygous mutations in SMO associated with anterior segment dysgenesis and morning glory syndrome. *Gene* **713**, 143973.
68. Choi, J.J.Y., Ting, C.-T., Trogrlic, L., Milevski, S.V., Familari, M., Martinez, G., and de Jongh, R.U. (2014). A role for smoothened during murine lens and cornea development. *PLoS ONE* **9**, e108037.

Supplemental Data

Bi-allelic Variations of *SMO* in Humans Cause a Broad Spectrum of Developmental Anomalies Due to Abnormal Hedgehog Signaling

Thuy-Linh Le, Yunia Sribudiani, Xiaomin Dong, Céline Huber, Chelsea Kois, Geneviève Baujat, Christopher T. Gordon, Valerie Mayne, Louise Galmiche, Valérie Serre, Nicolas Goudin, Mohammed Zarhrate, Christine Bole-Feysot, Cécile Masson, Patrick Nitschké, Frans W. Verheijen, Lynn Pais, Anna Pelet, Simon Sadedin, John A. Pugh, Natasha Shur, Susan M. White, Salima El Chehadeh, John Christodoulou, Valérie Cormier-Daire, R.M.W. Hofstra, Stanislas Lyonnet, Tiong Yang Tan, Tania Attié-Bitach, Wilhelmina S. Kerstjens-Frederikse, Jeanne Amiel, and Sophie Thomas

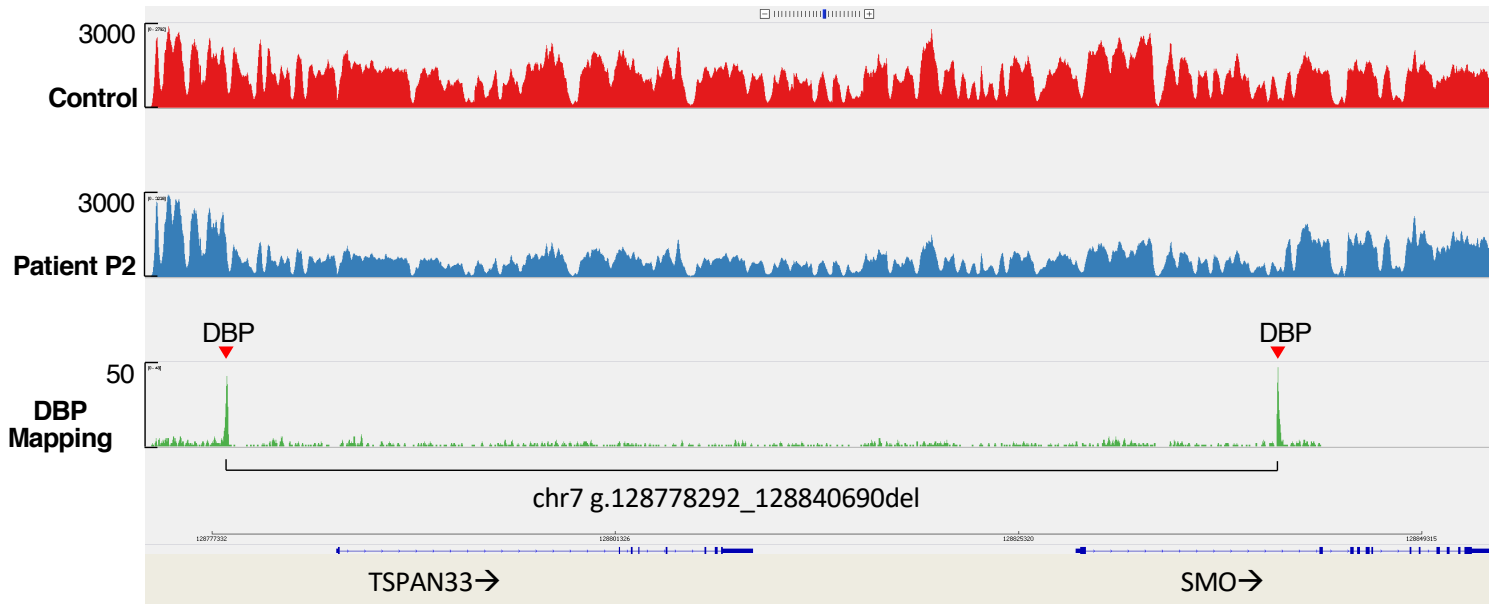


Figure S1: Quantitative visualization of sequencing read alignments. The sequencing data of a healthy control (red) and the patient P2 (blue) were aligned and mapped to the genomic position (GRCh37-hg19 genome assembly), showing a reduction by half of the number of reads in the deleted interval. DNA break points (DBP) were mapped by searching for read pairs that were aligned on the same chromosome with a relative distance of more than 500 bp and less than 10000 bp.

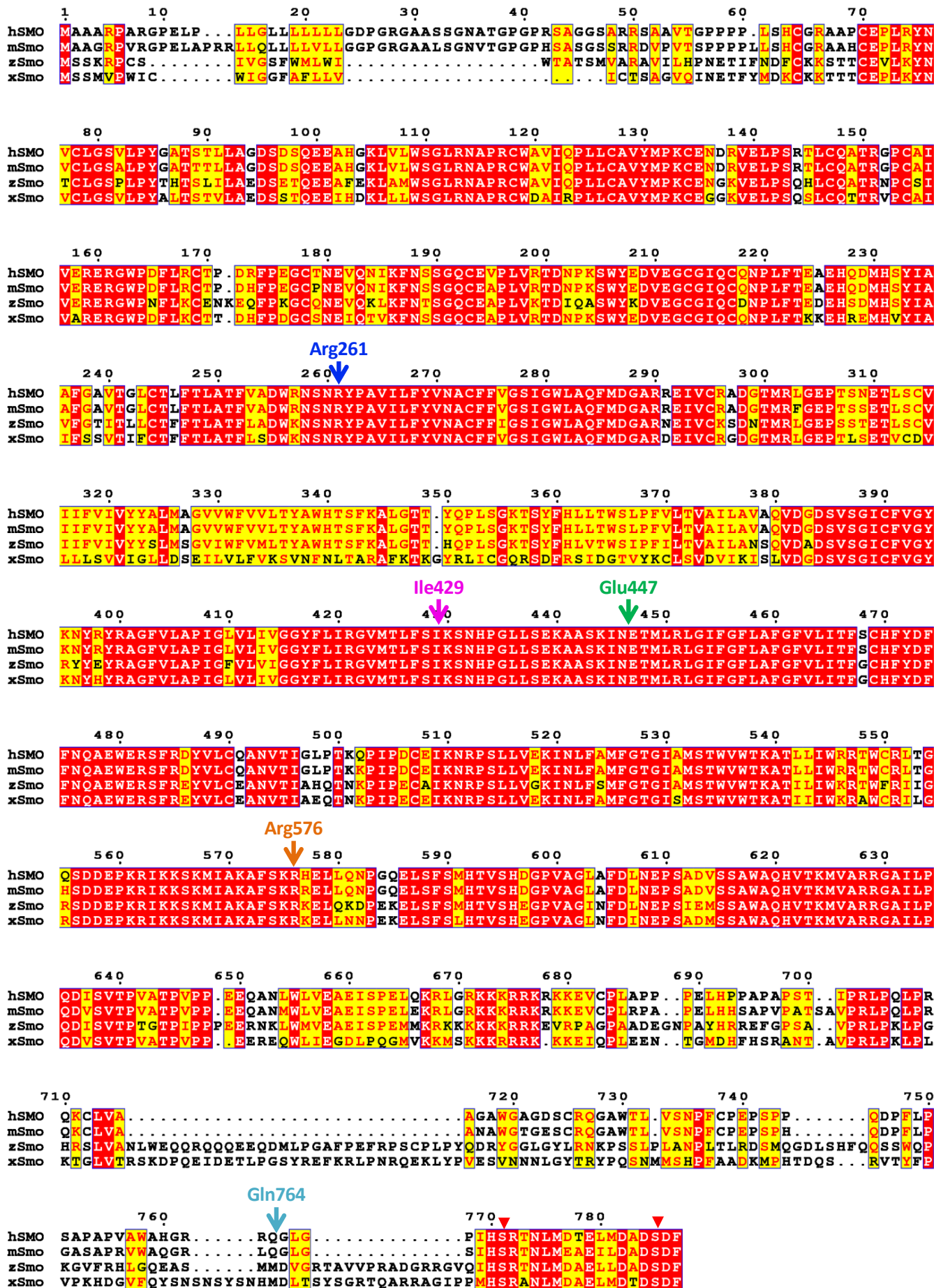


Figure S2: Sequence alignment of human (h), mouse (m), zebrafish (z), and xenopus (x) SMO protein. Mutated residues in affected individuals are highlighted. Red arrowheads point to phosphorylation sites Ser771 and Ser785. The graphic was rendered using ESPript server (<http://escript.ibcp.fr/EScript/>) with manual adjustments.

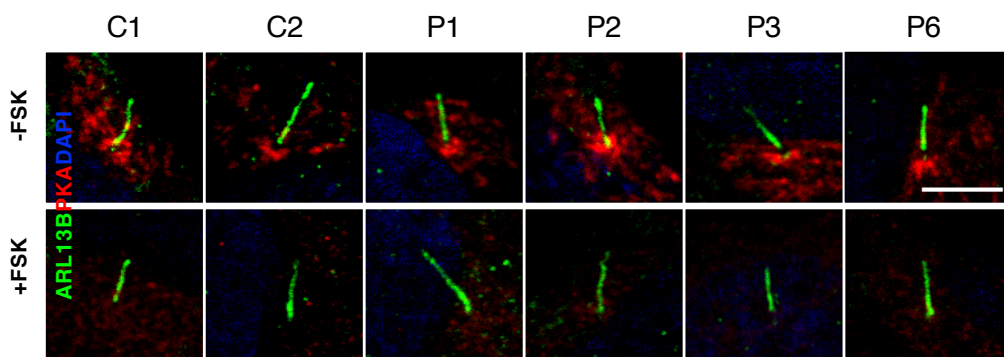


Figure S3: Normal PKA response to cAMP-mediated activation. Ciliogenesis-induced cells were fixed, incubated with anti-ARL13B antibody (Proteintech 17711-1-AP, 1:500) and anti-PKA^c (BD sciences, clone 5B Ruo, 1:500) at 4°C overnight and secondary antibody at RT for 1h, and mounted with DAPI. Representative images showing normal localisation of PKA at the PC base in untreated cells of control subjects and four patients (P1-3,P6) and subsequent dispersion of PKAc after 1-hour treatment with forskolin (FSK). Scale bar = 5μm.

Table S2: List of primers for DNA and cDNA sequencing

TARGETED SEQUENCES	FORWARD PRIMER	REVERSE PRIMER
GHSMO - EXON 1	CCGCGGCCGCCGAGGTCGTG	CTTTCCAAGGGTCCCCCATC
GHSMO - EXON 2	GTGATGGGCTGCAGTGTGGC	CTGGACCCCTGCCCTATAACCC
GHSMO - EXON 3	CCCTGCCATGCTACCTAGATAC	CTTCCCTCTGGCTCTCTTCC
GHSMO - EXON 4	GGGTCTGGGCTCAGTTAAG	CACTTCAGCCTCCTCCCTG
GHSMO - EXON 5	GGGGAGACCAGGTAGAGGGAG	CCCCCTCCCTCAAACTCACC
GHSMO - EXON 6	GGTGAGTTGAGGGAGGGGG	CAGCTCCCAGTACTGGCAGC
GHSMO - EXON 7	CCTCCCACTCACCCATCCTC	GTCCCAC TGACTTACTGCATC
GHSMO - EXON 8	GTGGGGCAGACTCTCTCCTC	GGTGGGTGGAGGTGGGTGTC
GHSMO - EXON 9	GGAAAGCCTCACCTGTCTAC	CCTAAAGATGGGTCCCAAG
GHSMO - EXON 10	GAGGCCCTTGGGAGCCTCCT	CCCAGCAGGCTGGGAGAGAC
GHSMO - EXON 11	GGCACTGACTATGGGAGGCAC	CAGCCCCGTACTCCAGTCCC
GHSMO - EXON 12	CAGGTTAACGTGCTCCCAGGG	CCTAGGGAAGCATGCTCGGTG
RT-HSMO-EXON3-8	GCATCCAGTGCCAGAACCGC	GCACAAAGCCAAGGCCAGG
RT-HSMO-EXON9-11	CCATGAGCACCTGGGTCTGG	CCACCATCTTGGTGACATGC
RT-HSMO-EXON11-12	CCCCAGGATATTCTGTAC	GAGTCTGCATCCATGAGTTC
CHR7: 128,801,354-128,829,881DEL	CTAGTCACCATCATTACCACC	AGAGAAACATCAGGCAGTTAAT
SMO_RTQRTPCR	GGGAGGCTACTTCCTCATCC	TGGTCTCGTTGATCTTGCTG
PTCH1_RTQRTPCR	GCTACTTACTCATGCTCGCC	TCCGATCAATGAGCACAGGC
GLI1_RTQRTPCR	AGAGGGGCCATGAAGCCAC	AAGGTCCCTCGTCCAAGCTG
GUSB_RTQRTPCR	GCGGTCGTGATGTGGTCTGT	GTGAGCGATCACCATCTTCAAGT
HPRT_RTQRTPCR	ACCAGTCAACAGGGGACATAAAAGTA	TTTGCCAGTGTCAATTATATCTTCCA

Table S3: List of antibodies for immunofluorescence (IF) and Western blot (WB) analyses

TARGETED PROTEIN	ANTIBODY	APPLICATION	PROVIDER	DILUTION
ACETYLATED A-TUBULIN	T6793, clone 6–11-B-1	IF	Sigma-Aldrich	1:1000
PERICENTRIN	ab4448	IF	Abcam	1:5000
SMO	Sc-166685	IF	Santa Cruz	1:100
GLI2	AF3526	IF	R&D Systems	1:200
ARL13B	17711-1-AP	IF	Proteintech	1:500
PKA CATALYTIC SUBUNIT	Clone 5B (RUO)	IF	BD Biosciences	1:500
GLI3	AF3690	WB	R&D Systems	1:1000
GAPDH	ab9458	WB	Abcam	1:5000